



The Powers of Relativistic Jets Depend on the Spin of Accreting Supermassive Black Holes

Yongyun Chen (陈永云)^{1,3}, Qiusheng Gu (顾秋生)^{2,3}, Junhui Fan (樊军辉)⁴, Hongyan Zhou (周宏岩)⁵, Yefei Yuan (袁业飞)⁵, Weimin Gu (顾为民)⁶, Qinwen Wu (吴庆文)⁷, Dingrong Xiong (熊定荣)⁸, Xiaotong Guo (郭晓通)², Nan Ding (丁楠)⁹, and Xiaoling Yu (俞效龄)²

¹ College of Physics and Electronic Engineering, Qujing Normal University, Qujing 655011, People's Republic of China; ynkmcy@yeah.net

² School of Astronomy and Space Science, Nanjing University, Nanjing 210093, People's Republic of China; qsgu@nju.edu.cn

³ Key Laboratory of Modern Astronomy and Astrophysics (Nanjing University), Ministry of Education, Nanjing 210093, People's Republic of China

⁴ Center for Astrophysics, Guangzhou University, Guangzhou 510006, People's Republic of China

⁵ University of Sciences and Technology of China, Chinese Academy of Sciences, Hefei 230026, People's Republic of China

⁶ Department of Astronomy, Xiamen University, Xiamen, Fujian 361005, People's Republic of China

⁷ School of Physics, Huazhong University of Science and Technology, Wuhan 430074, People's Republic of China

⁸ Yunnan Observatories, Chinese Academy of Sciences, Kunming 650011, People's Republic of China

⁹ School of Physical Science and Technology, Kunming University 650214, People's Republic of China; orient.dn@foxmail.com

Received 2020 December 7; revised 2021 March 2; accepted 2021 April 2; published 2021 May 28

Abstract

Theoretical models show that the power of relativistic jets of active galactic nuclei depends on the spin and mass of the central supermassive black holes, as well as the accretion. Here we report an analysis of archival observations of a sample of blazars. We find a significant correlation between jet kinetic power and the spin of supermassive black holes. At the same time, we use multiple linear regression to analyze the relationship between jet kinetic power and accretion, spin, and black hole mass. We find that the spin of supermassive black holes and accretion are the most important contributions to the jet kinetic power. The contribution rates of both the spin of supermassive black holes and accretion are more than 95%. These results suggest that the spin energy of supermassive black holes powers the relativistic jets. The jet production efficiency of almost all Fermi blazars can be explained by moderately thin, magnetically arrested accretion disks around rapidly spinning black holes.

Unified Astronomy Thesaurus concepts: Active galactic nuclei (16); Blazars (164)

1. Introduction

Blazars are a special subclass of active galactic nuclei (AGNs) whose jets point to the observer. Blazars are usually classified as flat-spectrum radio quasars (FSRQs) and BL Lac objects (BL Lacs) based on the equivalent width (EW) of the optical emission lines. The EW of FSRQs is larger than 5 Å, while BL Lacs have an EW < 5 Å (Stickel et al. 1991; Urry & Padovani 1995). Later, some authors used other physical parameters to distinguish FSRQs and BL Lacs. Ghisellini et al. (2011) used the ratio of the broad emission line to the Eddington luminosity to divide the FSRQs and BL Lacs, namely the accretion rate. They pointed out that FSRQs have $L_{\text{BLR}}/L_{\text{Edd}} \geq 5 \times 10^{-4}$, while BL Lacs have less than this value. This division between FSRQs and BL Lacs may imply that they have different accretion regimes (Sbarrato et al. 2014).

It is generally believed that the nonthermal radiation of the blazars originated from the relativistic jet. However, the formation of jets has always been an unsolved problem in astrophysics. In the theoretical models of jet formation, the jet power is coupled to the spin of the black hole (j), black hole mass (M), and magnetic field strength (B) that threads the horizon (Blandford & Znajek 1977; Macdonald & Thorne 1982; Thorne et al. 1986): $P_{\text{jet}} \propto j^2 M^2 B^2$. If the magnetic field is closely related to the luminosity of the accretion disk (Zamaninasab et al. 2014), then there will be a correlation between the jet power and the accretion disk

luminosity. Many authors have found this correlation (Rawlings & Saunders 1991; Celotti & Fabian 1993; Celotti et al. 1997; Maraschi & Tavecchio 2003; Celotti & Ghisellini 2008; Ghisellini et al. 2010, 2014; Sbarrato et al. 2012, 2014; Chen et al. 2015b, 2015c; Mukherjee et al. 2019). What's more, the jet power is larger than the luminosity of the accretion disk (Ghisellini et al. 2014), which implies that other physical parameters play an important role in determining jet power besides accretion (Meier 2002), such as the spin and black hole mass of supermassive black holes (SMBHs). In particular, it has often been speculated that the spin of a black hole is the main parameter in determining the jet power because spacetime dragging can twist the magnetic field lines (Blandford & Znajek 1977). Recently, Event Horizon Telescope (EHT) observations of M 87 at 1.3 mm (230 GHz) have revealed a ring-like structure on event horizon scales surrounding the SMBH, interpreted as the black hole "shadow" (Event Horizon Telescope Collaboration et al. 2019a, 2019b, 2019c, 2019d, 2019e, 2019f, hereafter Papers I–VI). At the same time, EHT observations of 3C 279 at 1.3 mm (230 GHz) have resolved the jet base in 3C 279 (Kim et al. 2020). These results suggest that relativistic jets in AGNs are closely related to black holes. Evidence for spin-enhanced jets has been reported for stellar mass black holes in X-ray binaries (Narayan & McClintock 2012). However, inadequate knowledge of the spin of the limited and inhomogeneous samples prevent one from drawing a firm conclusion.

Since the Fermi Large Area Telescope (LAT) was successfully launched in 2008, the research of blazars has entered a new era. In this paper, we use a large sample of Fermi blazars to study the relationship between jet powers and the spin of SMBHs. The samples are described in Section 2, the methods



Original content from this work may be used under the terms of the [Creative Commons Attribution 4.0 licence](#). Any further distribution of this work must maintain attribution to the author(s) and the title of the work, journal citation and DOI.

Table 1
The Sample of Fermi Blazars

Name [1]	z [2]	Type [3]	$\log L_{\text{disk}}$ [4]	$\log M_{\text{BH}}$ [5]	$\log L_{151}$ [6]	$\log L_{\gamma}^{\text{obs}}$ [7]	$\log L_{\text{J}}$ [8]	$\log B$ [9]	j [10]	$\log f_b$ [11]	$\log P_{\text{rad}}$ [12]	$\log P_{\text{jet}}$ [13]
1FGL J0846.9-2334	0.059	BZQ	43.18	8.3	39.29	44.03	41.19	3.93	0.08	-1.7	43.67	45.00
2FGL J1203.2 + 6030	0.065	BZB	43	8.6	39.56	43.99	41.45	3.68	0.09	-2.65	42.65	44.49
2FGL J1221.4 + 2814	0.103	BZB	43.08	8.6	40.3	45.28	42.08	3.7	0.18	-2.3	43.36	43.97
2FGL J1117.2 + 2013	0.138	BZB	42.95	8.6	40.29	45.16	42.07	3.67	0.19	-2.81	43.30	44.60
2FGL J1420.2 + 5422	0.153	BZB	43.26	8.3	40.86	44.89	42.56	3.95	0.34	-2.3	44.00	44.70
2FGL J0831.9 + 0429	0.174	BZB	43.65	8.5	41.05	45.69	42.71	3.89	0.3	-2.3	43.77	44.73
2FGL J1221.3 + 3010	0.184	BZB	43.08	8.6	39.9	45.62	41.74	3.7	0.12	-2.3	43.77	43.67
1FGL J0017.4-0510	0.226	BZQ	44.65	7.55	40.81	45.86	42.51	4.79	0.27	-2.46	43.98	46.49
1FGL J0422.0-0647	0.242	BZQ	44.49	7.47	40.38	45.17	42.14	4.81	0.2	-2.46	43.73	46.27
1FGL J0937.7 + 5005	0.276	BZQ	43.78	7.5	40.2	45.83	41.99	4.63	0.24	-2.38	43.64	46.18
2FGL J1125.6-3559	0.284	BZB	44.43	8.8	41.13	45.49	42.78	3.84	0.18	-2.65	43.50	44.59
1FGL J2237.2-3919	0.297	BZQ	44.78	7.86	41.11	45.5	42.77	4.59	0.28	-2.53	45.06	46.87
1FGL J1818.1 + 0905	0.354	BZQ	44.88	7.4	40.76	46.09	42.47	4.94	0.26	-2.46	44.11	45.08
1FGL J2334.3 + 0735	0.401	BZQ	45.73	8.37	41.59	46.09	43.17	4.43	0.2	-2.46	44.28	45.93
1FGL J1505.0 + 0328	0.409	BZQ	44.83	7.41	41	46.37	42.68	4.92	0.33	-2.59	44.49	45.95
1FGL J1549.3 + 0235	0.414	BZQ	45.78	8.67	41.65	46.49	43.22	4.23	0.17	-2.38	44.59	46.16
1FGL J1224.7 + 2121	0.434	BZQ	46.08	8.9	42.83	46.59	44.23	4.13	0.39	-2.53	45.49	46.32
1FGL J2117.8 + 0016	0.463	BZQ	44.78	7.745	41.3	46.23	42.93	4.67	0.36	-2.46	44.24	45.30
2FGL J0013.8 + 1907	0.477	BZB	43.78	8.3	40.51	45.72	42.26	4.06	0.19	-2.38	43.76	45.16
1FGL J0430.4-2509	0.516	BZQ	43.95	6.51	40.81	46.16	42.51	5.38	0.68	-2.38	43.77	44.80
1FGL J0714.0 + 1935	0.54	BZQ	44.78	7.62	41.68	47.17	43.25	4.76	0.54	-2.46	44.39	45.18
1FGL J1043.1 + 2404	0.559	BZB	44.68	8.09	41.61	46.34	43.19	4.41	0.4	-2.21	44.17	46.06
1FGL J2331.0-2145	0.563	BZQ	44.88	7.58	41.01	46.96	42.68	4.81	0.29	-2.46	44.83	45.90
1FGL J1514.7 + 4447	0.57	BZQ	44.3	7.67	41.08	46.45	42.74	4.62	0.38	-2.38	44.30	46.33
1FGL J0949.0 + 0021	0.585	BZQ	45.35	7.595	41.12	47.18	42.78	4.9	0.25	-2.65	45.01	47.22
1FGL J1642.5 + 3947	0.593	BZQ	45.95	8.88	43.22	47.35	44.56	4.11	0.58	-2.38	45.67	46.93
1FGL J2035.4 + 1100	0.601	BZQ	45.18	8	42.3	46.98	43.78	4.58	0.61	-2.46	44.94	46.38
1FGL J1023.6 + 3937	0.604	BZQ	45.88	8.95	42.79	46.47	44.19	4.05	0.4	-2.38	44.49	45.65
2FGL J1540.4 + 1438	0.606	BZB	44.56	8.5	42.97	46.26	44.34	4.09	0.91	-2.3	44.30	45.99
1FGL J0217.0-0829	0.607	BZQ	44.2	6.53	42.07	46.29	43.59	5.42	0.99	-2.53	44.34	45.99
1FGL J2344.6-1554	0.621	BZQ	45.32	8.32	41.56	46.8	43.15	4.38	0.25	-2.46	45.03	45.92
1FGL J0509.2 + 1015	0.621	BZQ	45.26	8.275	42.1	46.78	43.61	4.4	0.43	-2.46	44.66	45.58
1FGL J0102.8 + 5827	0.644	BZQ	45.65	8.57	42.4	47.21	43.86	4.27	0.39	-2.38	45.03	46.68
2FGL J1824.0 + 5650	0.664	BZB	44.91	8.5	42.92	47.17	44.37	4.16	0.85	-2.3	45.18	46.68
1FGL J0721.4 + 0401	0.665	BZQ	46.26	8.805	41.35	46.79	42.97	4.23	0.09	-2.53	45.23	46.28
1FGL J0840.8 + 1310	0.68	BZQ	45.73	8.495	43.63	46.63	44.9	4.34	0.93	-2.46	44.83	46.87
1FGL J1954.8-1124	0.683	BZQ	44.48	6.73	42.11	47.24	43.62	5.33	1	-2.38	44.80	45.49
1FGL J0956.9 + 2513	0.708	BZQ	45.88	8.465	42.26	46.63	43.74	4.4	0.33	-2.3	44.96	46.62
1FGL J1351.0 + 3035	0.712	BZQ	45.54	8.27	41.75	46.48	43.31	4.46	0.27	-2.46	44.83	46.54
1FGL J1159.4 + 2914	0.725	BZQ	45.56	8.375	43.2	47.5	44.54	4.39	0.83	-2.46	45.45	46.35
1FGL J1954.8 + 1402	0.743	BZQ	45.65	8.28	41.81	47.03	43.37	4.48	0.27	-2.38	45.20	46.83
1FGL J1830.1 + 0618	0.745	BZQ	46.35	8.775	42.28	47.42	43.76	4.27	0.22	-2.53	45.22	46.74
2FGL J0204.0 + 3045	0.761	BZB	45.73	8.8	41.63	46.74	43.21	4.12	0.16	-2.38	44.71	46.36
2FGL J2236.4 + 2828	0.79	BZB	45.62	8.85	42.1	47.47	43.61	4.06	0.25	-2.34	45.15	46.23
1FGL J2236.2 + 2828	0.79	BZQ	45.38	8.35	42.08	47.52	43.59	4.37	0.38	-2.38	45.22	46.23
1FGL J1848.5 + 3224	0.8	BZQ	45.65	8.04	42.17	47.47	43.66	4.65	0.44	-2.53	45.27	46.90
1FGL J1258.3 + 3227	0.806	BZQ	45.62	8.255	42.07	46.84	43.58	4.49	0.36	-2.53	45.04	46.73
1FGL J2315.9-5014	0.808	BZQ	44.65	7.68	41.95	46.8	43.48	4.69	0.67	-2.53	44.66	45.82
2FGL J2315.7-5014	0.811	BZB	44.68	8	41.95	46.71	43.48	4.47	0.57	-2.46	44.65	45.73
1FGL J0540.9-0547	0.838	BZQ	46.02	8.74	42.85	47.02	44.25	4.23	0.45	-2.53	45.32	46.88
1FGL J1106.5 + 2809	0.843	BZQ	45.2	8.85	41.22	46.96	42.86	3.97	0.13	-2.38	44.90	46.52
1FGL J0442.7-0019	0.845	BZQ	45.78	8.1	42.96	47.84	44.34	4.63	0.75	-2.53	45.71	46.47
1FGL J0456.4-3132	0.865	BZQ	45.48	8.195	41.58	46.83	43.16	4.5	0.25	-2.53	44.84	46.36
1FGL J0608.2-0837	0.87	BZQ	46.23	8.825	43.11	47.26	44.46	4.21	0.49	-2.46	45.32	46.82
2FGL J2152.4 + 1735	0.874	BZB	45.18	8.8	42.66	46.72	44.08	4.01	0.53	-2.3	44.67	45.19
1FGL J0102.2 + 4223	0.874	BZQ	45.78	8.205	41.47	47.26	43.07	4.56	0.19	-2.46	45.25	46.65
1FGL J0004.7-4737	0.88	BZQ	45.32	7.85	42.45	47.06	43.9	4.71	0.7	-2.59	44.64	45.85
1FGL J2025.9-2852	0.884	BZQ	45.05	8.34	41.88	46.94	43.42	4.31	0.37	-2.53	45.73	46.68
1FGL J1058.4 + 0134	0.888	BZQ	45.48	8.37	43.53	47.87	44.82	4.38	0.97	-2.59	45.61	46.57
1FGL J0957.7 + 5523	0.899	BZQ	45.65	8.45	43.48	47.93	44.78	4.36	0.91	-2.38	45.87	46.85
1FGL J0050.0-0446	0.922	BZQ	45.32	8.2	42.22	47.01	43.71	4.46	0.48	-2.38	44.89	46.58
2FGL J0434.1-2014	0.928	BZB	44.18	8	42.36	46.9	43.83	4.36	0.88	-2.38	44.57	45.70
1FGL J0654.3 + 4514	0.928	BZQ	45.26	8.17	42.44	47.85	43.9	4.47	0.6	-2.46	45.43	46.37

Table 1
(Continued)

Name [1]	z [2]	Type [3]	$\log L_{\text{disk}}$ [4]	$\log M_{\text{BH}}$ [5]	$\log L_{151}$ [6]	$\log L_{\gamma}^{\text{obs}}$ [7]	$\log L_j$ [8]	$\log B$ [9]	j [10]	$\log f_b$ [11]	$\log P_{\text{rad}}$ [12]	$\log P_{\text{jet}}$ [13]
1FGL J1342.7 + 5753	0.933	BZQ	45.78	8.42	42.02	46.95	43.54	4.41	0.29	-2.46	45.13	46.42
1FGL J1443.8 + 2457	0.939	BZQ	45.26	7.63	42.44	47.02	43.9	4.86	0.78	-2.3	44.64	46.73
1FGL J0830.5 + 2407	0.942	BZQ	46.35	8.7	42.8	47.57	44.2	4.33	0.38	-2.46	45.82	47.05
1FGL J1321.1 + 2214	0.943	BZQ	45.38	8.315	41.95	47	43.48	4.4	0.35	-2.53	45.03	45.74
2FGL J2247.2-0002	0.949	BZB	45.13	8.8	42.39	46.96	43.86	3.99	0.43	-2.38	44.69	45.53
1FGL J0203.5 + 3044	0.955	BZQ	44.48	8.02	41.87	47.16	43.41	4.41	0.57	-2.53	45.08	46.50
1FGL J1222.5 + 0415	0.966	BZQ	46.18	8.37	42.99	47.39	44.36	4.53	0.58	-2.46	45.94	47.35
1FGL J0043.6 + 3424	0.966	BZQ	45	8.01	41.57	47.24	43.15	4.53	0.35	-2.59	45.05	45.75
1FGL J1734.4 + 3859	0.975	BZQ	45.3	7.97	42.19	47.86	43.68	4.62	0.54	-2.53	45.40	46.04
1FGL J1310.6 + 3222	0.997	BZQ	45.95	8.57	43.18	48	44.53	4.34	0.67	-2.38	45.53	46.87
1FGL J0946.6 + 1012	1.006	BZQ	45.67	8.47	42.87	47.11	44.26	4.35	0.61	-2.46	45.20	46.09
1FGL J1359.1 + 5539	1.014	BZQ	45.13	8	41.74	47.25	43.3	4.57	0.39	-2.53	45.30	46.22
1FGL J0909.0 + 0126	1.026	BZQ	46.53	9.14	42.84	47.96	44.24	4.05	0.28	-2.53	45.96	47.28
1FGL J1709.6 + 4320	1.027	BZQ	45.18	7.92	42.11	47.48	43.61	4.63	0.55	-2.65	45.53	46.34
1FGL J0725.3 + 1431	1.038	BZQ	45.95	8.31	42.87	47.59	44.26	4.52	0.6	-2.59	45.80	46.94
2FGL J2206.6-0029	1.053	BZB	44.83	8.5	41.82	46.99	43.37	4.14	0.35	-2.38	44.72	46.26
1FGL J1317.8 + 3425	1.055	BZQ	46.03	9.14	43	47.19	44.37	3.95	0.4	-2.38	44.86	46.60
1FGL J1033.8 + 6048	1.064	BZQ	45.38	8.75	42.94	47.65	44.32	4.08	0.63	-2.59	45.03	46.40
1FGL J1224.2 + 5012	1.065	BZQ	46.56	8.66	41.56	47.53	43.15	4.4	0.11	-2.59	45.74	46.73
1FGL J1037.7-2820	1.066	BZQ	46.03	8.99	42.4	47.52	43.87	4.05	0.25	-2.46	45.47	46.33
1FGL J2219.3 + 1804	1.071	BZQ	45.18	7.645	42.04	47.1	43.55	4.83	0.6	-2.59	44.70	45.85
1FGL J1146.8 + 4004	1.088	BZQ	46.07	8.93	42.46	47.45	43.91	4.1	0.27	-2.46	45.57	46.59
1FGL J0608.0-1521	1.094	BZQ	45.56	8.09	42.42	47.99	43.88	4.59	0.55	-2.59	45.42	46.76
1FGL J1033.2 + 4116	1.117	BZQ	45.78	8.61	43.05	47.47	44.42	4.27	0.63	-2.59	45.45	46.19
1FGL J1152.1 + 6027	1.12	BZQ	45.95	8.94	42.23	47.44	43.72	4.07	0.23	-2.53	45.59	46.56
1FGL J2212.1 + 2358	1.125	BZQ	45.78	8.46	42.22	47.31	43.71	4.38	0.34	-2.53	44.93	46.95
1FGL J0407.5 + 0749	1.133	BZQ	45.78	8.65	42.73	47.22	44.14	4.24	0.47	-2.46	45.31	46.85
1FGL J0533.0 + 4825	1.16	BZQ	46.3	9.25	42.87	47.63	44.26	3.92	0.29	-2.53	45.68	46.56
1FGL J0048.0 + 2232	1.161	BZQ	45.26	8.34	41.74	47.72	43.3	4.35	0.3	-2.53	45.46	46.71
2FGL J2244.1 + 4059	1.171	BZQ	45.38	8.28	42.5	47.83	43.95	4.42	0.57	-2.59	45.41	46.82
1FGL J0237.9 + 2848	1.206	BZQ	46.26	9.22	43.4	48.24	44.71	3.94	0.49	-2.53	45.70	47.02
1FGL J2031.5 + 1219	1.213	BZQ	44.88	7.59	43.12	47.67	44.47	4.81	0.99	-2.81	45.20	45.98
1FGL J1016.2 + 3548	1.228	BZQ	46.35	9.1	42.66	47.48	44.09	4.04	0.26	-2.65	46.46	47.30
1FGL J1609.0 + 1031	1.232	BZQ	46.26	8.77	42.95	47.9	44.33	4.26	0.43	-2.46	45.63	47.19
1FGL J0654.4 + 5042	1.253	BZQ	44.98	8.325	42.41	47.96	43.87	4.3	0.61	-2.46	45.37	46.05
1FGL J0532.9 + 0733	1.254	BZQ	45.95	8.43	43.49	48.09	44.79	4.44	0.85	-2.59	46.02	46.95
1FGL J0438.8-1250	1.285	BZQ	45.8	8.66	42.78	47.6	44.18	4.24	0.49	-2.38	45.09	46.30
1FGL J1347.8-3751	1.3	BZQ	45.73	8.285	42.35	47.96	43.82	4.49	0.43	-2.46	45.34	47.01
1FGL J0941.2 + 2722	1.305	BZQ	45.71	8.63	41.87	47.52	43.41	4.24	0.22	-2.46	45.02	45.90
1FGL J1553.4 + 1255	1.308	BZQ	46.78	8.64	43.3	48.33	44.63	4.46	0.5	-2.46	45.58	46.34
1FGL J1802.5-3939	1.319	BZQ	46.18	8.595	43.67	48.51	44.94	4.37	0.84	-2.46	46.24	46.82
1FGL J1209.3 + 5444	1.344	BZQ	45.62	8.4	42.34	47.71	43.81	4.39	0.42	-2.59	45.88	46.75
2FGL J0334.2-4008	1.357	BZB	44.86	8.6	42.87	48.2	44.26	4.08	0.77	-2.76	45.74	46.85
1FGL J2145.4-3358	1.361	BZQ	45.35	8.31	41.87	47.69	43.41	4.39	0.33	-2.53	44.99	46.18
1FGL J1333.2 + 5056	1.362	BZQ	45.38	7.95	42.08	47.91	43.59	4.66	0.48	-2.65	45.53	46.11
1FGL J0058.0 + 3314	1.369	BZQ	45.18	7.99	41.8	47.75	43.35	4.58	0.4	-2.53	45.15	46.49
1FGL J0245.9-4652	1.385	BZQ	46.38	8.4	43.67	48.25	44.95	4.55	0.85	-2.46	46.06	47.12
1FGL J0257.8-1204	1.391	BZQ	46.35	9.22	42.15	47.49	43.65	3.96	0.15	-2.38	45.27	46.41
1FGL J1613.5 + 3411	1.4	BZQ	46.73	9.08	43.5	47.38	44.8	4.14	0.47	-2.3	45.29	47.07
1FGL J1033.8 + 6048	1.401	BZQ	45.71	9.09	43.22	48.04	44.56	3.91	0.58	-2.65	46.04	47.32
1FGL J1326.6 + 2213	1.403	BZQ	46.02	9.25	42.74	48.05	44.15	3.86	0.3	-2.53	45.97	47.30
1FGL J1550.7 + 0527	1.417	BZQ	46.08	8.98	43.61	47.49	44.89	4.07	0.71	-2.46	45.59	47.08
1FGL J0825.0 + 5555	1.418	BZQ	46.35	9.1	43.6	48.17	44.88	4.04	0.59	-2.59	46.02	47.34
1FGL J0252.8-2219	1.419	BZQ	45.5	9.4	43.26	48.42	44.59	3.65	0.55	-2.46	45.92	47.17
1FGL J1804.1 + 0336	1.42	BZQ	45.08	7.79	43.35	47.78	44.67	4.71	0.99	-2.65	45.90	46.54
1FGL J0041.9 + 2318	1.426	BZQ	45.62	9.01	42.68	47.75	44.1	3.95	0.39	-2.53	45.74	47.21
1FGL J2157.4 + 3129	1.448	BZQ	45.73	8.89	43.13	48.16	44.48	4.06	0.59	-2.53	45.73	46.65
1FGL J0919.6 + 6216	1.453	BZQ	46.01	8.93	43.3	47.94	44.62	4.09	0.59	-2.46	45.72	46.75
1FGL J1522.1 + 3143	1.484	BZQ	45.65	8.92	42.91	49.02	44.3	4.02	0.5	-2.46	45.90	47.04
1FGL J2322.0 + 3208	1.489	BZQ	45.73	8.705	43	47.74	44.37	4.19	0.59	-2.46	45.54	46.40
1FGL J1332.6-1255	1.492	BZQ	46.26	8.785	42.5	48.47	43.95	4.25	0.28	-2.65	46.14	46.94
1FGL J0011.1 + 0050	1.493	BZQ	45.56	8.445	42.14	47.45	43.64	4.34	0.35	-2.53	45.50	47.27
1FGL J1436.9 + 2314	1.548	BZQ	46.17	8.31	43.03	47.55	44.39	4.57	0.62	-2.38	45.39	46.46

Table 1
(Continued)

Name [1]	z [2]	Type [3]	$\log L_{\text{disk}}$ [4]	$\log M_{\text{BH}}$ [5]	$\log L_{151}$ [6]	$\log L_{\gamma}^{\text{obs}}$ [7]	$\log L_j$ [8]	$\log B$ [9]	j [10]	$\log f_b$ [11]	$\log P_{\text{rad}}$ [12]	$\log P_{\text{jet}}$ [13]
1FGL J1123.9 + 2339	1.549	BZQ	45.83	8.79	42.96	47.61	44.34	4.15	0.52	-2.53	45.45	46.39
1FGL J2229.7-0832	1.56	BZQ	46.48	8.62	43.03	48.79	44.4	4.41	0.46	-2.53	46.32	47.19
1FGL J0315.9-1033	1.565	BZQ	45.62	7.75	43.31	47.93	44.64	4.85	0.99	-2.53	45.44	46.90
1FGL J2110.0 + 0811	1.58	BZQ	46.05	8.82	41.92	47.97	43.45	4.18	0.18	-2.53	45.21	46.50
1FGL J1358.1 + 7646	1.585	BZQ	45.18	8.255	42.67	47.87	44.09	4.4	0.71	-2.65	45.57	46.85
1FGL J1133.1 + 0033	1.633	BZB	45.88	8.8	43.31	48.06	44.64	4.16	0.67	-2.59	45.75	46.49
1FGL J1016.1 + 0514	1.714	BZQ	45.65	7.99	43.09	48.72	44.45	4.69	0.88	-2.46	45.88	46.56
1FGL J1228.2 + 4855	1.722	BZQ	45.65	8.255	43.55	48.09	44.84	4.5	0.97	-2.46	45.61	46.23
2FGL J0629.3-2001	1.724	BZB	45.13	8.5	43.11	48.29	44.47	4.21	0.85	-2.38	45.85	46.58
1FGL J0254.2 + 5107	1.732	BZQ	46.02	8.74	43.12	48.42	44.47	4.23	0.56	-2.59	46.06	46.80
1FGL J0923.2 + 4121	1.732	BZQ	44.88	7.92	42.83	48.13	44.22	4.57	0.94	-2.53	45.47	46.00
1FGL J0104.4-2406	1.747	BZQ	45.91	8.91	42.23	47.91	43.72	4.08	0.24	-2.38	45.63	46.55
1FGL J1239.5 + 0443	1.761	BZQ	45.83	8.57	42.58	48.56	44.01	4.31	0.42	-2.65	46.81	47.58
1FGL J1012.7 + 2440	1.8	BZQ	46.13	7.795	42.34	48.42	43.81	4.93	0.48	-2.38	45.77	46.26
1FGL J1635.0 + 3808	1.813	BZQ	46.78	9.075	43.77	48.96	45.03	4.15	0.58	-2.59	47.69	48.06
1FGL J1504.4 + 1029	1.839	BZQ	46.18	8.94	43.62	49.76	44.9	4.12	0.7	-2.81	47.27	47.29
1FGL J2327.7 + 0943	1.841	BZQ	46.48	9.025	43.11	48.99	44.47	4.12	0.39	-2.46	46.42	47.77
1FGL J1112.8 + 3444	1.956	BZQ	46.28	8.78	42.84	48.16	44.24	4.26	0.39	-2.3	45.89	46.57
1FGL J1225.8 + 4336	2.001	BZQ	46.41	8.825	43.59	48.26	44.88	4.25	0.67	-2.71	46.41	47.10
1FGL J0433.5 + 3230	2.011	BZQ	46.56	9.185	42.47	47.83	43.92	4.03	0.18	-2.53	45.35	46.89
2FGL J0438.8-4521	2.017	BZB	45.26	8.5	42.41	48.22	43.87	4.24	0.49	-2.38	45.66	46.78
1FGL J0023.0 + 4453	2.023	BZQ	45.43	7.78	42.88	48.25	44.27	4.79	0.89	-2.65	45.85	46.77
1FGL J0325.9 + 2219	2.066	BZQ	46.78	9.33	43.25	48.52	44.58	3.97	0.32	-2.46	46.32	47.27
1FGL J0856.6 + 2103	2.098	BZQ	46.42	9.865	43.39	48.32	44.71	3.51	0.31	-2.65	45.73	46.34
1FGL J1959.3-4241	2.178	BZQ	46.16	8.98	42.38	48.52	43.84	4.09	0.23	-2.46	46.03	46.69
1FGL J2120.9 + 1901	2.18	BZQ	45.78	7.75	43.61	48.56	44.9	4.89	1	-2.53	45.98	46.98
1FGL J2135.8-4957	2.181	BZQ	46.12	8.355	43.04	48.61	44.4	4.53	0.62	-2.71	46.42	47.30
1FGL J0920.9 + 4441	2.189	BZQ	46.71	9.29	43.77	49.38	45.03	3.98	0.54	-2.46	46.64	47.83
1FGL J1539.7 + 2747	2.191	BZQ	45.65	8.47	42.65	48	44.08	4.34	0.52	-2.46	45.66	46.11
1FGL J0245.4 + 2413	2.243	BZQ	46.32	9.1	43.51	48.48	44.8	4.04	0.56	-2.59	46.29	47.41
1FGL J0157.5-4613	2.287	BZQ	45.78	8.25	42.88	48.46	44.27	4.53	0.66	-2.59	45.99	46.64
1FGL J1152.2-0836	2.367	BZQ	46.28	9.38	43.26	48.51	44.59	3.83	0.39	-2.53	45.98	47.31
1FGL J1344.2-1723	2.506	BZQ	46.03	9.12	43.06	49.02	44.42	3.96	0.43	-2.76	46.19	46.14
1FGL J1345.4 + 4453	2.534	BZQ	46.02	8.98	43.21	48.8	44.55	4.06	0.53	-2.59	46.60	47.29
1FGL J0912.3 + 4127	2.563	BZQ	46.35	9.32	43.67	48.53	44.94	3.89	0.56	-2.38	45.99	46.95
1FGL J1441.7-1538	2.642	BZQ	46.19	8.49	44.05	48.63	45.26	4.44	0.98	-2.46	46.55	47.90
1FGL J0911.0 + 2247	2.661	BZQ	46.18	8.7	42.85	48.72	44.24	4.29	0.43	-2.71	46.37	47.20
1FGL J0746.6 + 2548	2.979	BZQ	46.48	9.23	43.3	49.14	44.63	3.98	0.41	-2.71	47.35	48.40
1FGL J0806.2 + 6148	3.033	BZQ	46.52	9.07	43.78	49.2	45.04	4.1	0.65	-2.65	47.18	48.16
1FGL J1624.7-0642	3.037	BZQ	46.56	8.23	44.29	48.54	45.47	4.71	1	-2.59	45.96	47.04

Note. The first column is the name of Fermi blazars; the second column is the redshift; the third column is the class of Fermi blazars; the fourth column is the Logarithm of disk luminosity (in units of erg s^{-1}); the fifth column is the Logarithm of the black hole mass (in units of solar mass); the sixth column is the Logarithm of the radio luminosity in 151 MHz (in units of erg s^{-1}); the seventh column is the Logarithm of the observational γ -ray luminosity (in units of erg s^{-1}); the eighth column is the Logarithm of the beam power estimated using Equation (1) (in units of erg s^{-1}); the ninth column is the Logarithm of the magnetic field strength of the accretion disk estimated using Equation (2) (in units of Gauss); the tenth column is the spin of the black hole estimated using Equation (3); the eleventh column is the Logarithm of the beaming factor; the twelfth column is the radiation jet power from Ghisellini et al. (2014); and the thirteenth column is the jet kinetic power from Ghisellini et al. (2014); in units of erg s^{-1} .

are presented in Section 3, the results and discussions are in Section 4, and the conclusions are in Section 5. The cosmological parameters $H_0 = 70 \text{ km s}^{-1} \text{ Mpc}^{-1}$, $\Omega_m = 0.3$, and $\Omega_\Lambda = 0.7$ have been adopted in this work.

2. The Sample

We collect a large sample of blazars detected by the Fermi LAT (Abdo et al. 2010; Ackermann et al. 2011). First, we consider that these blazars have spectral observation data (Shaw et al. 2012, 2013). The sample contains 229 FSRQs and 475 BL Lacs. We only use BL lacs with broad emission lines because there are no or only weak emission lines. This is the

largest sample of γ -ray-detected sources with measured broad emission lines and black hole masses. We use these broad emission lines, such as H α , H β , Mg II, and C IV, to estimate the luminosity of the broad line region (L_{BLR}) using the standard templates (Francis et al. 1991; Celotti et al. 1997). We calculate the accretion disk luminosity (Calderone et al. 2013) using $L_{\text{disk}} = 10L_{\text{BLR}}$, with an average uncertainty of 0.3 dex. Second, our sample has also been detected by the TIFR Giant metrewave radio telescope Sky Survey (TGSS; Intema et al. 2017) at 150 MHz. This ensures that we can calculate the beam power using the flux of 150 MHz. Finally, we have a sample containing 166 Fermi blazars (144 FSRQs and 22 BL Lacs). The samples are presented in Table 1.

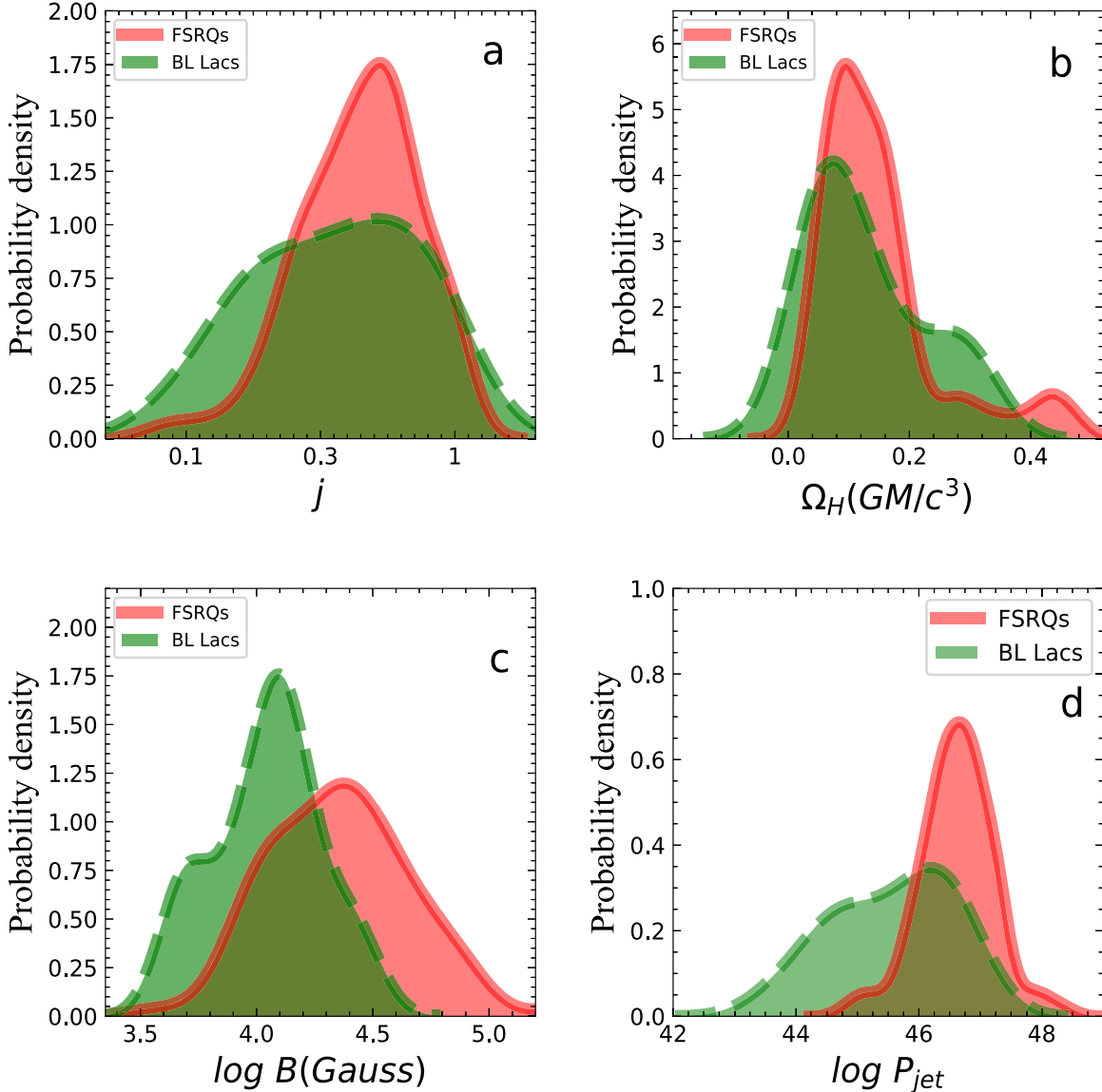


Figure 1. The density distribution of relevant quantities. (a) The density distribution of the spin of SMBHs for FSRQs and BL Lacs. (b) The density distribution of the angular velocity of SMBHs for FSRQs and BL Lacs. (c) The density distribution of the magnetic field of the accretion disk for FSRQs and BL Lacs. (d) The density distribution of the jet kinetic power for FSRQs and BL Lacs. The red histogram is for the FSRQs. The green dashed histogram is for the BL Lacs. The average values of the distributions are $\langle j_{\text{FSRQs}} \rangle = 0.50 \pm 0.23$, $\langle j_{\text{BL Lacs}} \rangle = 0.44 \pm 0.27$, $\langle \Omega_{\text{H}}(GM/c^3)_{\text{FSRQs}} \rangle = 0.15 \pm 0.10$, $\langle \Omega_{\text{H}}(GM/c^3)_{\text{BL Lacs}} \rangle = 0.13 \pm 0.09$, $\langle \log B_{\text{FSRQs}} \rangle = 4.37 \pm 0.32$, $\langle \log B_{\text{BL Lacs}} \rangle = 4.04 \pm 0.23$, $\langle \log P_{\text{jet}}(\text{FSRQs}) \rangle = 46.62 \pm 0.60$, and $\langle \log P_{\text{jet}}(\text{BL Lacs}) \rangle = 45.56 \pm 0.93$.

3. The Method

3.1. The Beam Power

According to the theoretical model described (Willott et al. 1999), the relationships between the beam power and radio luminosity are

$$L_j \approx 1.7 \times 10^{45} f^{3/2} \left(\frac{L_{151}}{10^{44} \text{ erg s}^{-1}} \right)^{6/7} \text{ erg s}^{-1}, \quad (1)$$

where L_{151} is the radio luminosity at 151 MHz in units of erg s^{-1} . The range of f is $1 \leq f \leq 20$. This equation was used to estimate the beam power of FR II radio galaxies. We also use this equation to estimate the beam power of blazars, which is believed to be a good approximation, since blazars

have radio properties similar to FR II radio galaxies (Cao 2003; Chen et al. 2015a, 2015b). Many authors use this formula to estimate the beam power of blazars (Cao 2003; Wu & Cao 2008; Godfrey & Shabala 2013; Fan & Wu 2018, 2019). In this paper, we use the low limit $f=1$ in most cases (Cao 2003). The luminosity is calculated using the formula $L_{\nu} = 4\pi d_L^2 S_{\nu}$, $d_L(z) = \frac{c}{H_0}(1+z) \int_0^z [\Omega_{\Lambda} + \Omega_m(1+z')^3]^{-1/2} dz'$, where d_L is the luminosity distance (Venters et al. 2009). We make a K -correction for the observed flux using $S_{\nu} = S_{\nu}^{\text{ob}}(1+z)^{\alpha-1}$, with $\alpha=0.8$ (Cassaro et al. 1999). We use the luminosity of 151 MHz to calculate the beam power through above Equation (1). The values of the luminosity of 151 MHz and the beam power are listed in columns (6) and (8) of Table 1, respectively. A Λ CDM cosmology with $H_0=70 \text{ km s}^{-1} \text{ Mpc}^{-1}$, $\Omega_m=0.27$, and $\Omega_{\Lambda}=0.73$ is adopted.

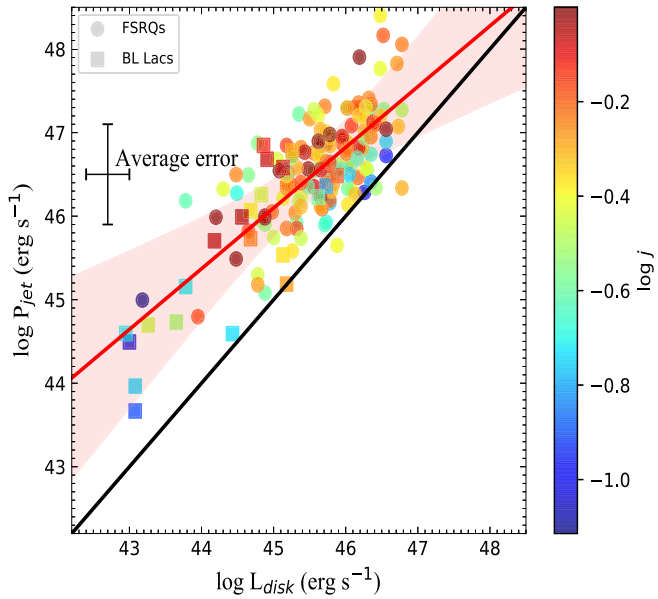


Figure 2. The jet kinetic power as a function of the disk luminosity of SMBHs for FSRQs and BL Lacs. The gray large filled circles are FSRQs, while the filled squares are BL Lacs. The red line shows the least-squares best fit ($\log P_{\text{jet}} = 0.73 \log L_{\text{disk}} + 13.39$). The black line is the equality line ($P_{\text{jet}} = L_{\text{disk}}$). Shaded red areas correspond to the 3σ confidence bands. The color bar indicates the spin of the SMBHs. The average error bar is indicated (the uncertainty of L_{disk} is 0.30 dex; the uncertainty of P_{jet} is 0.47 dex).

3.2. The Spin of Supermassive Black Holes and the Magnetic Field of the Accretion Disk

The total magnetic field strength of the accretion disk can be calculated using the following formula (Daly 2019),

$$\begin{aligned} \left(\frac{B}{10^4 \text{ G}} \right) &= \left(\frac{B}{B_{\text{Edd}}} \right) \left(\frac{\kappa_B^2}{M_8} \right)^{1/2} \\ \left(\frac{B}{B_{\text{Edd}}} \right) &= \left(\frac{L_{\text{bol}}}{g_{\text{bol}} L_{\text{Edd}}} \right)^{A/2} \\ \left(\frac{B}{10^4 \text{ G}} \right) &= \left(\frac{L_{\text{bol}}}{g_{\text{bol}} L_{\text{Edd}}} \right)^{A/2} \left(\frac{\kappa_B^2}{M_8} \right)^{1/2}, \end{aligned} \quad (2)$$

where B_{Edd} is the Eddington magnetic field strength in units of 10^4 G , $B_{\text{Edd},4} \equiv \kappa_B M_8^{-1/2}$, where $\kappa_B \approx 6$ (Rees 1984; Blandford 1990), and M_8 is the black hole mass in units of $10^8 M_\odot$. A was defined by Daly et al. (2018), $A = \alpha/(\alpha + b)$, α and b are the coefficients of the fundamental plane of black hole activity, where $A = 0.43$ (Merloni et al. 2003). L_{bol} is the bolometric luminosity (Netzer 1990), $L_{\text{bol}} = 10L_{\text{BLR}}$, and L_{Edd} is the Eddington luminosity, $L_{\text{Edd}} = 1.3 \times 10^{38} (M_{\text{BH}}/M_\odot)$. The spin of the black hole can be estimated using the following formula (Daly 2019),

$$\begin{aligned} \frac{f(j)}{f_{\max}} &= \left(\frac{L_j}{g_i L_{\text{Edd}}} \right) \left(\frac{L_{\text{bol}}}{g_{\text{bol}} L_{\text{Edd}}} \right)^{-A} \\ j &= \frac{2\sqrt{f(j)/f_{\max}}}{f(j)/f_{\max} + 1}, \end{aligned} \quad (3)$$

where L_j is the beam power, and $g_i = 0.1$ and $g_{\text{bol}} = 1$ are used (Daly 2019). The black hole spins obtained using this method

can be compared with those obtained using other methods, such as the X-ray reflection method (Reynolds 2014). The spin values of GX 339-4 are 0.94 ± 0.02 (Miller et al. 2009) and $0.95^{+0.03}_{-0.05}$ (García et al. 2009) using the X-ray reflection method, and the spin obtained using the method of Daly (2019) is 0.92 ± 0.06 . The spin obtained using the method of Daly is consistent with those obtained with the X-ray reflection method. Because of the limitation of the observations, it is very difficult to directly measure the spin of large samples using the X-ray reflection method. Therefore, we use the method of Daly to measure the spin for our samples. The accretion disk magnetic field strength values of $\sim 10^4 \text{ G}$ are also reported using other methods (Mikhailov et al. 2015). Thus, the accretion disk magnetic field strengths obtained here are similar to the values obtained using other methods. We use Equations (2) and (3) to estimate the magnetic field strength of the accretion disk and the spin of black hole, respectively. The values of the magnetic field strength and the spin of black hole are listed in columns (9) and (10) of Table 1.

3.3. The Intrinsic γ -Ray Luminosity

We estimate the intrinsic γ -ray luminosity using the formula (Nemmen et al. 2012)

$$L_\gamma = f_b L_\gamma^{\text{obs}} \text{ erg s}^{-1}, \quad (4)$$

where L_γ^{obs} is the observational γ -ray luminosity. f_b is the beaming factor, and f_b is estimated as $1 - \cos(1/\Gamma)$, where Γ is the bulk Lorentz factor. The bulk Lorentz factor comes from Ghisellini et al. (2014). L_γ^{obs} is the observed γ -ray luminosity from the catalog of LAT (Abdo et al. 2010; Ackermann et al. 2011). The values of L_γ^{obs} and f_b are listed in columns (7) and (11) of Table 1, respectively. The values of the radiation jet power and the jet kinetic power come from Ghisellini et al. (2014). Ghisellini et al. (2014) used a simple one-zone leptonic model to get the radiation jet power and the jet kinetic power. They are listed in columns (12) and (13) of Table 1, respectively.

4. Results and Discussions

4.1. The Distribution of Physical Parameters

The density distributions of the spin of SMBHs and the magnetic field strength of the accretion disks are shown in Figure 1. The average spins of SMBHs for FSRQs and BL Lacs are $\langle j_{\text{FSRQs}} \rangle = 0.50 \pm 0.23$ and $\langle j_{\text{BL Lacs}} \rangle = 0.44 \pm 0.27$, respectively. The average values of the magnetic field strength of the accretion disk for FSRQs and BL Lacs are $\langle \log B_{\text{FSRQs}} \rangle = 4.37 \pm 0.32$ and $\langle \log B_{\text{BL Lacs}} \rangle = 4.04 \pm 0.23$, respectively. We find that the spin of SMBHs and the magnetic field strength of FSRQs are higher than those of BL Lacs. Moreover, the jet kinetic power of FSRQs is larger than that of BL Lacs. These results suggest that the spin of SMBHs and accretion can power the relativistic jets. The magnetic fields play a critical role in jet formation and accretion disk physics (Zamaninasab et al. 2014; Blandford et al. 2019). At the same time, the angular velocity is also an important physical parameter, $\Omega_H = j(c^3/2GM)/(1 + \sqrt{1 - j^2})$ (Tchekhovskoy et al. 2010). Tchekhovskoy et al. (2010) found that there is a significant correlation between the angular velocity and jet power. Thus, we study the distribution of the angular velocity.

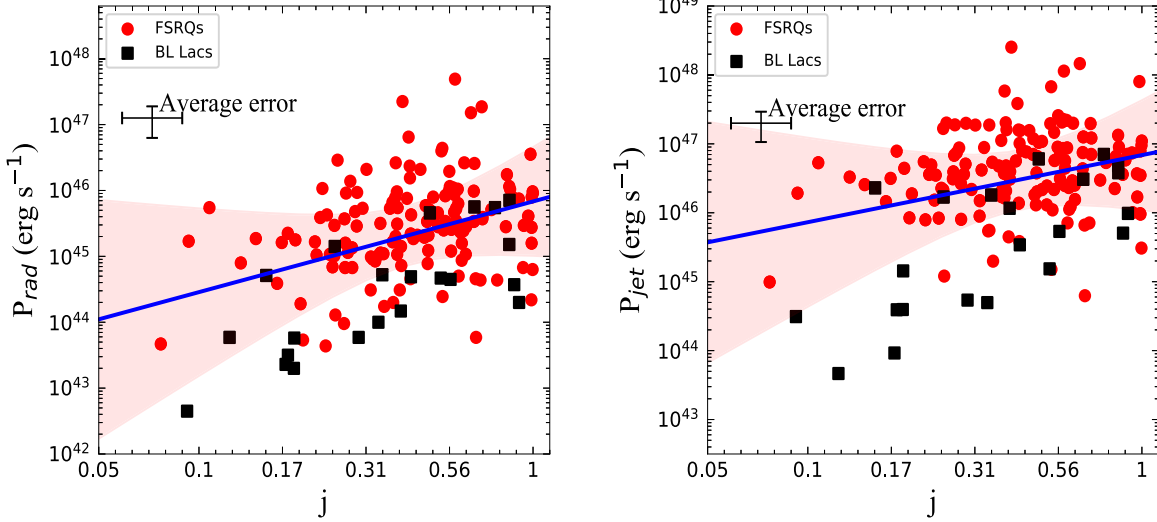


Figure 3. Radiative jet power (left panel) and jet kinetic power (right panel) vs. the spin of SMBHs for FSRQs and BL Lacs, respectively. The radiative jet power and jet kinetic power are estimated through a simple one-zone leptonic model (Ghisellini & Tavecchio 2009). The large filled circles are FSRQs, while filled squares are BL Lacs. Shaded red areas correspond to the 3σ confidence bands. The two blue lines are the best least-squares fits of $\log P_{\text{rad}} = 1.38, \log j + 45.83$, and $\log P_{\text{jet}} = 0.97, \log j + 46.83$. The upper left corner shows the average error bar. The average uncertainty of P_{rad} is a factor of 1.7; the average uncertainty of P_{jet} is a factor of 3.

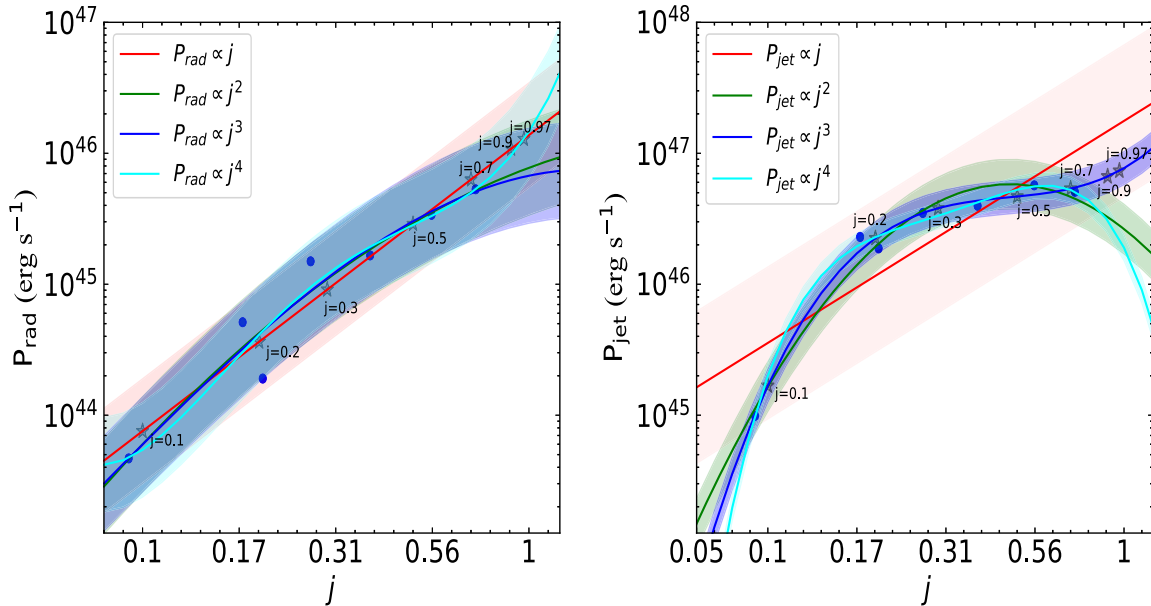


Figure 4. Radiative jet power (left panel) and jet kinetic power (right panel) vs. the spin of black holes in different regimes for whole samples, respectively. Shaded red areas correspond to the 2σ confidence bands. For reference, the following values are for the black hole spin, $j = [0.1, 0.2, 0.3, 0.5, 0.7, 0.9, 0.97]$. The blue solid dot is the median in different regimes of spin. The stars are the reference values. We use polynomial regression to fit the median. The red line is the first-order fitting. The green line is the second-order fitting, the blue line is the third-order fitting, and the cyan line is the fourth-order fitting.

Table 2
The Results of Correlation Analysis for Fermi Blazars

Parameter 1	Parameter 2	Pearson r, p	Spearman r, p	Kendall r, p
$\log j$	$\log P_{\text{rad}}$	0.40, 7.16×10^{-8}	0.34, 5.56×10^{-6}	0.23, 4.76×10^{-6}
	$\log P_{\text{jet}}$	0.31, 5.50×10^{-5}	0.21, 0.007	0.14, 0.008
$\log \Omega_{\text{H}}(GM/c^3)$	$\log P_{\text{rad}}$	0.37, 7.42×10^{-7}	0.34, 5.56×10^{-6}	0.24, 4.76×10^{-6}
	$\log P_{\text{jet}}$	0.28, 0.0002	0.21, 0.007	0.14, 0.008

Note. The r is the correlation coefficient; p is the significance level ($p < 0.01$).

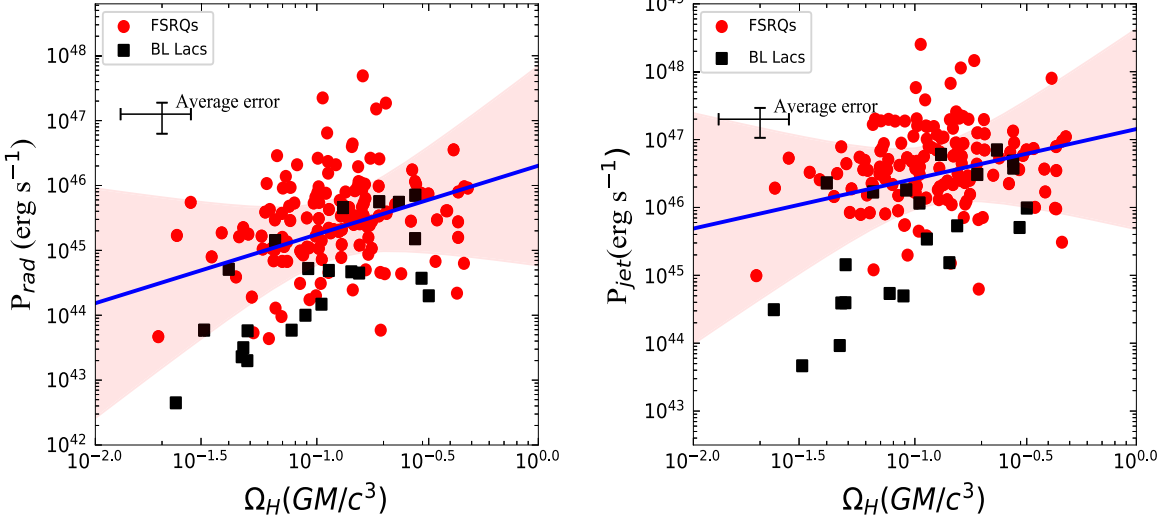


Figure 5. Radiative jet power (left panel) and jet kinetic power (right panel) vs. the angular velocity of the SMBH horizon Ω_H along the abscissa for FSRQs and BL Lacs, respectively. Different symbols correspond to the different type of blazars. Shaded red areas correspond to the 3σ confidence bands. The two blue lines are the best least-squares fits of $\log P_{\text{rad}} = 1.06$, $\log(\Omega_H GM/c^3) + 46.31$ and $\log P_{\text{jet}} = 0.73$, $\log(\Omega_H GM/c^3) + 47.15$, respectively. The upper left corner shows the average error bars.

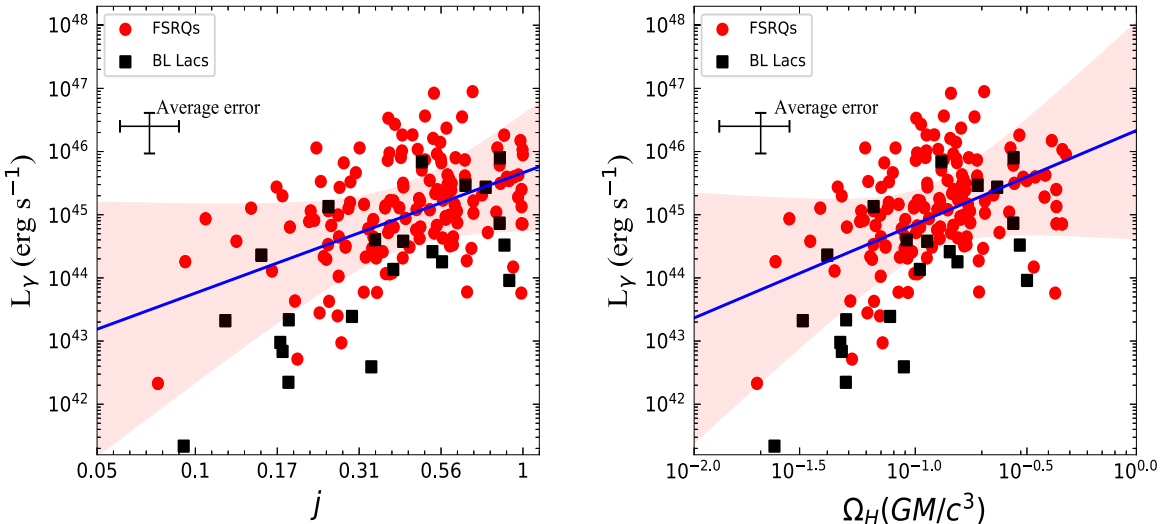


Figure 6. The intrinsic γ -ray luminosity as a function of the spin of SMBHs (left panel) and the angular velocity of the black hole horizon Ω_H (right panel) for FSRQs and BL Lacs, respectively. Different symbols correspond to the different type of blazars. Shaded red areas correspond to the 3σ confidence bands. The two blue lines are the best least-square fits of $\log L_\gamma = 1.91$, $\log j + 45.66$ and $\log L_\gamma = 1.48 \log(\Omega_H GM/c^3) + 46.33$, respectively. The upper left corner shows the average error bars.

The mean values of the angular velocities of FSRQs and BL Lacs are $\langle \Omega_H(GM/c^3)_{\text{FSRQs}} \rangle = 0.15 \pm 0.10$, and $\langle \Omega_H(GM/c^3)_{\text{BL Lacs}} \rangle = 0.13 \pm 0.09$, respectively. The angular velocity of FSRQs is larger than that of BL Lacs. The AGNs with fast rotating black holes have powerful relativistic jets (Blandford 1990). At the same time, our results also support larger values of the spin of SMBHs, which is similar to what has been found in models of SMBH evolution and growth through mergers (Volonteri et al. 2005, 2007, 2013). The average values of the spin of SMBHs of FSRQs are $\langle j_{\text{FSRQs}} \rangle = 0.50 \pm 0.23$, which are consistent with the values simulated by using general relativistic magnetohydrodynamics from a thin disk (Soares & Nemmen 2020). Our results are consistent with the merger-driven evolution of SMBHs. The density distribution of the jet kinetic power is shown in Figure 1. The average values of the jet kinetic power for FSRQs and BL Lacs are $\langle \log P_{\text{jet}} | \text{FSRQs} \rangle = 46.62 \pm 0.60$ and

$\langle \log P_{\text{jet}} | \text{BL Lacs} \rangle = 45.56 \pm 0.93$, respectively. The FSRQs have a higher jet kinetic power than the BL Lacs. At the same time, we find that FSRQs have a higher spin of SMBHs than BL Lacs. These results imply that AGNs with higher jet kinetic power tend to have a higher spin of the SMBHs, which is consistent with the numerical simulation (Tchekhovskoy et al. 2011; Avara et al. 2016). Therefore, the evidence suggests that relativistic jets are powered directly by the spin energy of the accreting SMBHs.

4.2. The Relation between the Jet Kinetic Power and the Accretion Disk Luminosity

The relationship between the jet kinetic power and the accretion disk luminosity is studied (see Figure 2). The color bar indicates the value of the spin of SMBHs. The black line indicates $P_{\text{jet}} = L_{\text{disk}}$. The red line is the best-fit correlation ($\log P_{\text{jet}} = 0.73 \log L_{\text{disk}} + 13.39$) and almost always lies above the equality line. The jet kinetic power is slightly higher than

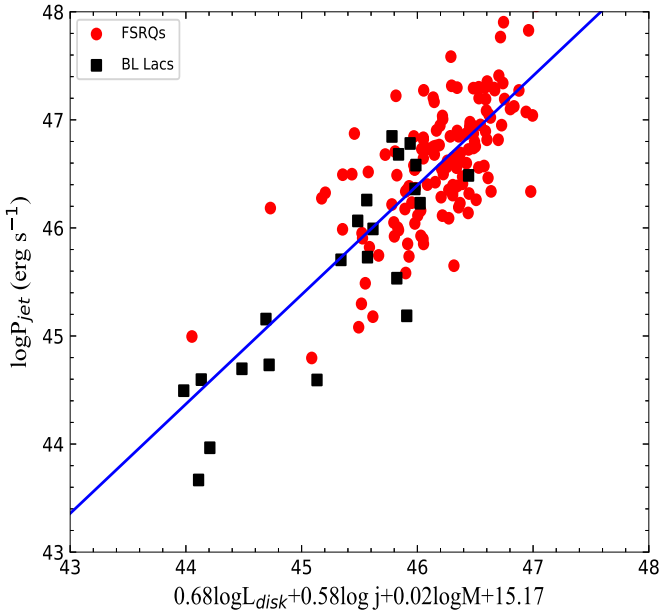


Figure 7. The jet kinetic power as a function of accretion disk luminosity and spin of SMBHs and the black hole mass for FSRQs and BL Lacs. Different symbols correspond to the different type of blazars. The blue line shows the best-fitting function.

the luminosity of the accretion disk. We find that objects with high spin tend to have a high jet kinetic power. Our result further suggests that the jet may come from the spin of the SMBHs in addition to the accretion. This result is in agreement with the general relativistic magnetohydrodynamic (GRMHD) simulations (Tchekhovskoy et al. 2011). The larger the spin, the stronger the relativistic jet produced by the accretion system.

4.3. The Relation between the Jet Power and Spin of the Supermassive Black Holes

Figure 3 shows the relationship between the radiative jet power (P_{rad}) and the jet kinetic power (P_{jet}) as a function of the spin of SMBHs (j) for 166 Fermi blazars, respectively. There are two significant correlations among P_{rad} and P_{jet} and j are $\log P_{\text{rad}} = 1.38 \log j + 45.83$ (with $p = 7.16 \times 10^{-8}$) and $\log P_{\text{jet}} = 0.97 \log j + 46.83$ (with $p = 5.50 \times 10^{-5}$), respectively. At the same time, we also use Kendall and Spearman tests to analyze these correlations beside Pearson (see Table 2), and confirm significant correlations between them. Our results are consistent with the theoretical model (Blandford & Znajek 1977) and numerical simulations (Tchekhovskoy et al. 2012). The magnetohydrodynamic numerical simulations suggest that the rapidly spinning black holes can produce strong relativistic jets (Meier 2001; Nemmen et al. 2007). GRMHD simulations suggested that a spinning Kerr black hole can produce the powerful jets (Event Horizon Telescope Collaboration et al. 2019e; Porth et al. 2019; Liska et al. 2020). Parfrey et al. (2019) described the first direct plasma-kinetic simulations of the Blandford-Znajek process, in which a plasma-filled magnetosphere mediates the extraction of a black hole's rotational energy and the launching of a relativistic jet. Therefore, these observational evidences imply that the relativistic jets are directly enhanced by the spin of SMBHs.

GRMHD simulations showed that the jet power varies as steeply as the fourth power of the black hole angular rotation

rate when the spin of the black hole is greater than 0.5 (McKinney 2005a, 2005b), i.e., $P \propto \Omega_H^4$, where $\Omega_H \propto \alpha/r_H$ and r_H is the radius of the horizon, therefore, $P \propto \alpha^4$. Based on numerical analysis and calculations, Tanabe & Nagataki (2008) found that P increases as α^4 at large values of α when higher-order corrections are included. Tchekhovskoy et al. (2010) studied the relationship between the different regions of spin and jet power. They found $P \propto \Omega_H^4 \propto (\alpha/r_H)^2$ when the accretion disk is thin. However, the jet power dependence becomes much steeper when the accretion disk is thick, $P \propto \Omega_H^4$ or even $P \propto \Omega_H^6$. We re-examine the relationship between the jet power and the median of spin of black holes in different regimes. Figure 4 shows the relationship between the radiative jet power and jet kinetic power as a function of the median of spin of the black hole. In the left panel of Figure 4 there is no obvious difference in all the fittings. In the right panel of Figure 4, the third-order fitting is the best. From Figure 4, the jet power has a steep dependence on the spin, $P \propto j^3$ or $P \propto j^4$. Our results are consistent with the GRMHD simulations. Because the redshift of our sample is mainly from 0 to 2.5, the mass of the black hole is from $10^{7.5}$ to $10^{9.5} M_\odot$. At the same time, our samples lack low-luminosity AGNs. Therefore, our results may be biased and should be tested with a larger sample in the future. In particular, low-luminosity AGNs should be included.

The theoretical model suggested that if jet power depends on the spin of a SMBH, a relationship should exist between the jet power and the angular velocity of the SMBH horizon (Tchekhovskoy et al. 2010). Figure 5 shows the relationship between the radiative jet power and jet kinetic power, as well as the angular velocity of SMBHs. We also find significant correlations between them: $\log P_{\text{rad}} = 1.06$, $\log(\Omega_H GM/c^3) + 46.31$ (with $p = 7.42 \times 10^{-7}$), and $\log P_{\text{jet}} = 0.73$, $\log(\Omega_H GM/c^3) + 47.15$ (with $p = 0.0002$). The so-called spin paradigm suggests that the fast rotating black holes in AGNs can produce powerful relativistic jets (Blandford 1990). Our results confirm this theoretical model.

The γ -ray luminosity is a good indicator of jet power. In order to avoid the beaming effect, we use the beaming factor (f_b) to correct γ -ray luminosity (Nemmen et al. 2012; $L_\gamma = f_b L_\gamma^{\text{obs}}$). Figure 6 shows the relationship between the intrinsic γ -ray luminosity and the spin of SMBHs, as well as the angular velocity of SMBHs, respectively. There are two significant correlations between them: $\log L_\gamma = 1.91$, $\log j + 45.66$ (with $p = 4.47 \times 10^{-11}$) and $\log L_\gamma = 1.48$, $\log(\Omega_H GM/c^3) + 46.33$ (with $p = 1.01 \times 10^{-9}$), respectively. We also find that the slope of $\log L_\gamma - \log j$ is close to 2. This result is also consistent with the theoretical model of Blandford & Znajek (1977) and the numerical simulations of Tchekhovskoy et al. (2012). These evidences further confirm that the spin of SMBHs enhances the relativistic jets.

The theoretical model shows that the jet mainly comes from accretion, spin, and black hole mass (Blandford & Znajek 1977). In order to quantify the contribution of the accretion, spin, and black hole mass to jet power, we further investigate the connection between the properties of jets and the accretion, spin of SMBHs, and black hole mass. We use a multiple linear regression analysis to get the relation between the jet kinetic power and the accretion disk luminosity, the spin of SMBHs, and black hole mass (Figure 7): $\log P_{\text{jet}} = 0.68$, $\log L_{\text{disk}} + 0.58$, $\log j + 0.02$, and $\log M + 15.17$. Due to dimensional differences, we use standardized coefficients to define the

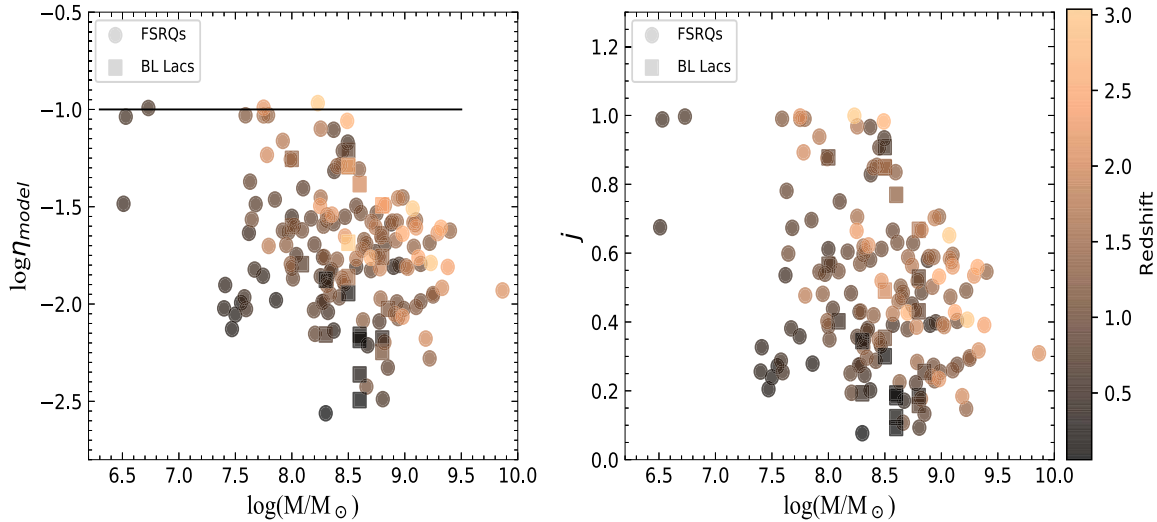


Figure 8. The jet production efficiency of the MAD model (left panel) and the spin of SMBHs (right panel) as a function of the mass of SMBHs for FSRQs and BL Lacs. The gray large filled circles are FSRQs, while the filled squares are BL Lacs. The black line corresponds to the limiting efficiency assuming the maximum allowed spin and the disk thickness of $h = 0.13$ in Equation (1). The color bar indicates the redshift.

contribution rates. The standardized coefficients of accretion, spin, and black hole mass are 0.737, 0.184, and 0.017, respectively. We separately define the contribution rates of accretion, spin, and black hole mass to the jet power as follows: $\varepsilon_{\text{accretion}} = 0.737/(0.737 + 0.184 + 0.017) \times 100\% = 78.57\%$; $\varepsilon_j = 0.184/(0.737 + 0.184 + 0.017) \times 100\% = 19.61\%$; and $\varepsilon_{\text{Mass}} = 0.017/(0.737 + 0.184 + 0.017) \times 100\% = 1.81\%$. The contribution rates of both the spin of SMBHs and accretion are 98.18%. These results suggest that the spin of SMBHs and accretion are the main contributions to the jet kinetic power (Sikora et al. 2007; Contopoulos et al. 2014).

GRMHD models have suggested that the magnetically arrested disks (MAD) around a rapidly spinning SMBH can produce strong relativistic jets (McKinney et al. 2012, 2013). In the Blandford-Znajek mechanism (Blandford & Znajek 1977), if the jet power scales as $P_{\text{jet}} \propto B^2 j^2$, then the MAD state leads to the maximum jet power. The jet power is larger than the disk luminosity (Ghisellini et al. 2014), which is in agreement with the MAD expectations. The most promising model for Fermi blazars is the GRMHD simulations of moderately thin MADs pointed out by Avara et al. (2016). According to the thin MAD model, the jet production efficiency in the thin MAD model is given by

$$\eta_{\text{model}} \approx 400 \text{ per cent } \omega_H^2 \left(1 + \frac{0.3\omega_H}{1 + 2h^4} \right)^2 h^2, \quad (5)$$

where $\omega_H \equiv j/r_H$ is the black hole rotation frequency, $r_H = 1 + \sqrt{1 - j^2}$ is the horizon radius, and $h \approx H/R$ is disk thickness. We use the spin of the SMBHs and the disk thickness ($h = 0.13$; Avara et al. 2016) to estimate the jet production efficiency in the thin MAD model through Equation (5).

The jet production efficiency in the thin MAD model as a function of black hole mass for FSRQs and BL Lacs is shown in Figure 8. The horizontal black line is the limiting efficiency assuming a black hole with the maximum spin, $j = 0.998$, and a disk thickness of $h = 0.13$. We find that there is only one object with high jet production efficiencies that cannot be explained by the thin MAD model. This object has higher accretion rate

than other sources, which may lead to the high jet production efficiency. At the same time, this object also has higher redshift ($z = 3.037$) than other sources. The sustained accretion of cold gas at high redshift tends to maximize the magnitude of spins (Dubois et al. 2014).

We can see that lower-spin objects tend to have high-mass SMBHs (see Figure 8). Such a tendency has been found in King et al. (2008). This result is consistent with the hypothesis that high-mass SMBHs were built from more isotropic chaotic accretion or the merging of smaller black holes (Volonteri et al. 2005; Sesana et al. 2014; Fiacconi et al. 2018). At the same time, some authors found that there is a relation between spin and redshift (Dubois et al. 2014). They found that the spins are close to the maximum value when the redshift is larger than 2, while the spins decrease as the black hole masses increase when the redshift is between 1 and 2. However, we did not find a relation between the spin and redshift. Our results are consistent with the GRMHD simulations (Soares & Nemmen 2020).

5. Conclusions

We use a large sample of Fermi blazars to study the relation between jet kinetic power and spin of SMBHs. Our main results are as follows.

(i) There is a significant correlation between jet kinetic power and the spin of SMBHs, which is consistent with theoretical models and numerical simulations.

(ii) We find that there is a significant correlation between jet kinetic power and accretion disk luminosity, which suggest a tight connection between the jet and accretion. At the same time, the jet kinetic power is greater than the accretion disk luminosity, which may indicate that the accretion is not enough to explain the jet kinetic power for Fermi blazars.

(iii) Using multiple linear regressions to analyze the relationship between the jet kinetic power and accretion, spin, and black hole mass, we find that the spin of SMBHs and accretion are the most important contribution to the jet kinetic power. The contribution rates of both the spin of SMBHs and

accretion are more than 95%. These results suggest that the spin energy of SMBHs powers the relativistic jets.

(iv) Our spin estimates are consistent with the results from models for the cosmological merger-driven evolution of SMBHs.

(v) Magnetically arrested, moderately thin accretion disks around a rapidly spinning SMBHs are able to explain the energetics of the majority of Fermi blazars.

We are very grateful to the referee for the very helpful comments and suggestions. The work was support from the research project of Qujing Normal University (2105098001/094). This work is supported by the youth project of Yunnan Provincial Science and Technology Department (2103010006). This work is supported by the National Natural Science Foundation of China (NSFC 11733001). This work is supported by the National Key Research and Development Program of China (No. 2017YFA0402703) and the National Natural Science Foundation of China (grant Nos. 11733002 and 11773013). N.D. thanks for the support of scientific research fund of Yunnan Provincial Education Department (2021J0715).

ORCID iDs

- Yongyun Chen (陈永 云) <https://orcid.org/0000-0001-5895-0189>
 Junhui Fan (樊军 辉) <https://orcid.org/0000-0002-5929-0968>
 Hongyan Zhou (周宏 岩) <https://orcid.org/0000-0003-1956-9021>
 Weimin Gu (顾为 民) <https://orcid.org/0000-0003-3137-1851>
 Dingrong Xiong (熊定 荣) <https://orcid.org/0000-0002-6809-9575>
 Xiaotong Guo (郭晓 通) <https://orcid.org/0000-0002-2338-7709>

References

- Abdo, A. A., Ackermann, M., Ajello, M., et al. 2010, *ApJS*, 188, 405
 Ackermann, M., Ajello, M., Allafort, A., et al. 2011, *ApJ*, 743, 171
 Avara, M. J., McKinney, J. C., & Reynolds, C. S. 2016, *MNRAS*, 462, 636
 Blandford, R., Meier, D., & Readhead, A. 2019, *ARA&A*, 57, 467
 Blandford, R. D. 1990, in Saas-Fee Advanced Course of the Swiss Society for Astrophysics and Astronomy: Active Galactic Nuclei, ed. T. J. L. Courvoisier & M. Mayor (Berlin: Springer), 161
 Blandford, R. D., & Znajek, R. L. 1977, *MNRAS*, 179, 433
 Calderone, G., Ghisellini, G., Colpi, M., & Dotti, M. 2013, *MNRAS*, 431, 210
 Cao, X. W. 2003, *ApJ*, 599, 147
 Cassaro, P., Stanghellini, C., Bondi, M., et al. 1999, *A&AS*, 139, 601
 Cavagnolo, K. W., McNamara, B. R., Nulsen, P. E. J., et al. 2010, *ApJ*, 720, 1066
 Celotti, A., & Fabian, A. C. 1993, *MNRAS*, 264, 228
 Celotti, A., & Ghisellini, G. 2008, *MNRAS*, 385, 283
 Celotti, A., Padovani, P., & Ghisellini, G. 1997, *MNRAS*, 286, 415
 Chen, Y. Y., Zhang, X., Xiong, D. R., et al. 2015a, *Ap&SS*, 357, 100
 Chen, Y. Y., Zhang, X., Xiong, D. R., & Yu, X. L. 2015b, *AJ*, 150, 8
 Chen, Y. Y., Zhang, X., Zhang, H. J., & Yu, X. L. 2015c, *MNRAS*, 451, 4193
 Contopoulos, I., Gabuzda, D., & Kyla, S. N. 2014, The Formation and Disruption of Black Hole Jets (Berlin: Springer)
 Daly, R. A. 2019, *ApJ*, 886, 37
 Daly, R. A., Stout, D. A., & Mysliwiec, J. N. 2018, *ApJ*, 863, 117
 Dubois, Y., Volonteri, M., & Silk, J. 2014, *MNRAS*, 440, 1590
 Event Horizon Telescope Collaboration, Akiyama, K., et al. 2019a, *ApJL*, 875, L1
 Event Horizon Telescope Collaboration, Akiyama, K., et al. 2019b, *ApJL*, 875, L2
 Event Horizon Telescope Collaboration, Akiyama, K., et al. 2019c, *ApJL*, 875, L3
 Event Horizon Telescope Collaboration, Akiyama, K., et al. 2019d, *ApJL*, 875, L4
 Event Horizon Telescope Collaboration, Akiyama, K., et al. 2019e, *ApJL*, 875, L5
 Event Horizon Telescope Collaboration, Akiyama, K., et al. 2019f, *ApJL*, 875, L6
 Fan, X. L., & Wu, Q. 2018, *ApJ*, 869, 133
 Fan, X. L., & Wu, Q. 2019, *ApJ*, 879, 107
 Fiacconi, D., Sijacki, D., & Pringle, J. E. 2018, *MNRAS*, 477, 3803
 Francis, P. J., Hewett, P. C., Foltz, C. B., et al. 1991, *ApJ*, 373, 465
 García, J. A., Steiner, J. F., McClintock, J. E., et al. 2009, *ApJ*, 813, 84
 Ghisellini, G., & Tavecchio, F. 2009, *MNRAS*, 397, 985
 Ghisellini, G., Tavecchio, F., Foschini, L., et al. 2010, *MNRAS*, 402, 497
 Ghisellini, G., Tavecchio, F., Foschini, L., & Ghirlanda, G. 2011, *MNRAS*, 414, 2674
 Ghisellini, G., Tavecchio, F., Maraschi, L., Celotti, A., & Sbarato, T. 2014, *Natur*, 515, 376
 Godfrey, L. E. H., & Shabala, S. S. 2013, *ApJ*, 767, 12
 Intema, H. T., Jagannathan, P., Mooley, K. P., & Frail, D. A. 2017, *A&A*, 598, A78
 Kim, J. Y., Krichbaum, T. P., Broderick, A. E., et al. 2020, *A&A*, 640, A69
 King, A. R., Pringle, J. E., & Hofmann, J. A. 2008, *MNRAS*, 385, 1621
 Liska, M., Tchekhovskoy, A., & Quataert, E. 2020, *MNRAS*, 494, 3656
 Macdonald, D., & Thorne, K. S. 1982, *MNRAS*, 198, 345
 Maraschi, L., & Tavecchio, F. 2003, *ApJ*, 593, 667
 McKinney, J. C. 2005a, arXiv:astro-ph/0506368
 McKinney, J. C. 2005b, *ApJL*, 630, L5
 McKinney, J. C., Tchekhovskoy, A., & Blandford, R. D. 2012, *MNRAS*, 423, 3083
 McKinney, J. C., Tchekhovskoy, A., & Blandford, R. D. 2013, *Sci*, 339, 49
 Meier, D. L. 2001, *ApJL*, 548, L9
 Meier, D. L. 2002, *NewAR*, 46, 247
 Merloni, A., Heinz, S., & Di Matteo, T. 2003, *MNRAS*, 345, 1057
 Mikhailov, A. G., Gnedin, Y. N., & Belonovsky, A. V. 2015, *Ap*, 58, 157
 Miller, J. M., Reynolds, C. S., Fabian, A. C., Miniutti, G., & Gallo, L. C. 2009, *ApJ*, 697, 900
 Mukherjee, S., Mitra, K., & Chatterjee, R. 2019, *MNRAS*, 486, 1672
 Narayan, R., & McClintock, J. E. 2012, *MNRAS*, 419, L69
 Nemmen, R. S., Bower, R. G., Babul, A., & Storchi-Bergmann, T. 2007, *MNRAS*, 377, 1652
 Nemmen, R. S., Georganopoulos, M., Guiriec, S., et al. 2012, *Sci*, 338, 1445
 Netzer, H. 1990, in Saas-Fee Advanced Course of the Swiss Society for Astrophysics and Astronomy: Active Galactic Nuclei, ed. T. J.-L. Courvoisier & M. Mayor (Berlin: Springer), 57
 Parfrey, K., Philippov, A., & Cerutti, B. 2019, *PRL*, 122, 035101
 Porth, Q., Chatterjee, K., Narayan, R., et al. 2019, *ApJS*, 243, 26
 Rawlings, S., & Saunders, R. 1991, *Natur*, 349, 138
 Rees, M. J. 1984, *ARA&A*, 22, 471
 Reynolds, C. S. 2014, *SSRv*, 183, 277
 Sbarato, T., Ghisellini, G., Maraschi, L., & Colpi, M. 2012, *MNRAS*, 421, 1764
 Sbarato, T., Padovani, P., & Ghisellini, G. 2014, *MNRAS*, 445, 81
 Sesana, A., Barausse, E., Dotti, M., & Rossi, E. M. 2014, *ApJ*, 792, 25
 Shaw, M. S., Romani, R. W., Cotter, G., et al. 2012, *ApJ*, 748, 49
 Shaw, M. S., Romani, R. W., Cotter, G., et al. 2013, *ApJ*, 764, 135
 Sikora, M., Stawarz, L., & Lasota, J. P. 2007, *ApJ*, 658, 815
 Soares, G., & Nemmen, R. 2020, *MNRAS*, 495, 981
 Soltan, A. 1982, *MNRAS*, 200, 115
 Stickel, M., Padovani, P., Urry, C. M., Fried, J. W., & Kuehr, H. 1991, *ApJ*, 374, 431
 Tanabe, K., & Nagataki, S. 2008, *Phys. Rev. D*, 78, 024004
 Tchekhovskoy, A., McKinney, J. C., & Narayan, R. 2012, *JPhCS*, 372, 012040
 Tchekhovskoy, A., Narayan, R., & McKinney, J. C. 2010, *ApJ*, 711, 50
 Tchekhovskoy, A., Narayan, R., & McKinney, J. C. 2011, *MNRAS*, 418, L79
 Thorne, K. S., Price, R. H., & MacDonald, D. A. 1986, Black Holes: The Membrane Paradigm (New Haven, CT: Yale Univ. Press)
 Urry, C. M., & Padovani, P. 1995, *PASP*, 107, 803
 Venters, T. M., Pavlidou, V., & Reyes, L. C. 2009, *ApJ*, 703, 1939
 Volonteri, M., Madau, P., Quataert, E., & Rees, M. J. 2005, *ApJ*, 620, 69
 Volonteri, M., Sikora, M., & Lasota, J. P. 2007, *ApJ*, 667, 704
 Volonteri, M., Sikora, M., Lasota, J. P., & Merloni, A. 2013, *ApJ*, 775, 94
 Willott, C. J., Rawlings, S., Blundell, K. M., & Lacy, M. 1999, *MNRAS*, 309, 1017
 Wu, Q. W., & Cao, X. W. 2008, *ApJ*, 687, 156
 Zamaninasab, M., Clausen-Brown, E., Savolainen, T., & Tchekhoskoy, A. 2014, *Natur*, 510, 126